Contents

1 Introduction

brmbrum 10 μm. The interaction of plasma with solid materials is of large importance for basic research studying the properties and behavior of hot plasmas. It is also important because of its possible applications in future fusion devices.

For example, in tokamaks used in *magnetic confinement fusion*, the plasma diffuses despite the magnetic gradient from the inner parts towards the outer parts of the tokamak. Consequently it reaches its wall and interacts with it. This is one example of the occurrence of plasma-wall interaction, which is intensively studied.

In the most common scheme of indirectly driven *inertial confinement fusion* we can see another example of plasma-wall interaction: The fusion *pellet* is inserted in the hohlraum, the inner surface of which is irradiated with laser beams to produce a plasma which interacts with the pellet.

The *laser–produced plasma* is a plasma generated using an intensive laser beam. The laser beam impinges on a solid target, typically a thin foil, where the matter is ionized and a plasma jet perpendicular to the target is produced. This represents a very efficient tool for investigating the plasma-wall interactions, because the expanding plasma jets can produce different interaction scenarios.

A very efficient diagnostics of such plasmas is based on the x-ray emission spectrometry.

The aim of this document is to describe the laser-plasma wall interaction experiments performed in PALS laboratory, which are directed to the acquistion of experimental data necessary for verification of theoretical models of plasma wall interactions and which should contribute to the understanding this phenomena.

The main diagnostic tool in those experiment was the *vertical-geometry Johann spectrometer* (VJS), as described further, which records the high-resolution, spatially resolved spectral data on an x-ray film.

The processing of the recorded spectra from VJS was the main part of my bachelor work. It consisted of calibrating the scanner and developing a software package for spectra reconstruction. During the research project I investigated the possibilities of using theretical spectra for plasma diagnostics and developed a new code for spectra comparison.

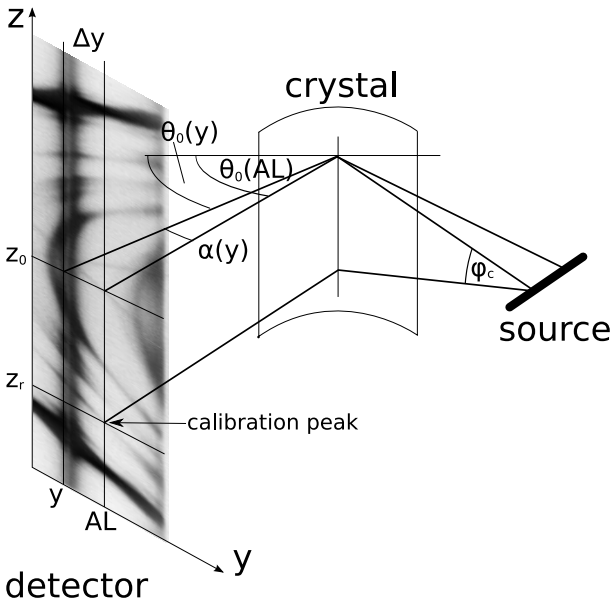

Figure 1.1: Schematic drawing of the VJS setup.

2 Elements of plasma radiation

The radiation emitted from hot dense plasmas is probably the most important diagnostic tool for these plasmas, because it carries information about the local plasma conditions. For short life-time plasmas, that we focus on in this thesis, the x-ray radiation is a very efficient diagnostic tool.[1]

The emission spectrum is produced by electron transitions, which can be classified with respect to the initial and the final transition states to *free-free*, *free-bound*, and *bound-bound* transitions. It is obvious that the photons emitted during the first two types of processes contribute to the *continuous spectrum*, while the latter process produces photons with discrete energy spectrum and therefore contributes to the *line spectrum*.

2.1 Line spectrum

The *line spectrum* occurs only in plasmas where ions are not fully stripped. In hot dense plasmas, that we are concerned, this is true only for the intermediate and high-Z plasmas.

The main process contributing to the line spectrum is the *spontaneous decay* in which an excited ion decays into a lower, usually ground state, emitting a photon with energy corresponding to the difference between the two electron states. The energies of those lines are given by the Bohr formula,

$$E = \frac{Z^2 e^3}{2a_0}\left(\frac{1}{n_{\mathrm{l}}^2} - \frac{1}{n_{\mathrm{u}}^2}\right), \tag{2.1}$$

where n_l and n_u are the principal quantum numbers of the lower and the upper state of the transition.

For the hydrogen-like ions (that is ions with only one bound electron left), the lines are organized into *series* according to the final state of the transition. The series are denoted by names, as seen in table 2.1. The lines from each series are denoted with a Greek letter in its subscript, e.g. Ly_α refers to $n_{\mathrm{l}} = 1$ and $n_{\mathrm{u}} = 2$.

series	abbrev.	n_{l}
Lyman	Ly	1
Balmer	Ba	2
Paschen	Pa	3
Brackett	Br	4
	...	

Table 2.1: Names of spectroscopic series

2.2 Satellite lines

Satellite lines constitute another part of the line spectrum. Usually they appear as low intensity lines near strong *parent* lines. They are caused by the decay of double– or multiply–excited ion.

If one of the excited electrons of a multiply-excited ion decays into a lower state, it emits a photon with energy similar to that emitted from the same transition in a single-excited ion. The presence of another excited electron, so called *spectator*, slightly modifies the electric potential of the ion and thus the energy of the transition levels and the wavelengths of the emitted photon.

This means that for each configuration of states of *spectator* electrons, there is a separate satellite line.

Near the Ly_α transition in hydrogen-like ions, the satellite lines corresponding to different states of the spectator electron are distinguished by the capital letters. In our measurements we have focused on the J satellite, which is produced with the spectator electron in one of the $2p$ states.

The main diagnostic advantage of satellite lines is their sensitivity to plasma parameters (electron density and temperature) and their small reabsorption compared to the resonance line photons.

Each photon emitted during radiative decay can be reabsorbed by the inverse process, the *resonant photoabsorption*. The rate of this process (the number of photons of given energy absorbed per unit time per unit volume) is proportional to the density of ions in the lower state of the corresponding transition.

This means that a photon emitted due to a decay of single excited ion into its ground state can be easily reabsorbed because the density of ions in the ground state is relatively large. In contrast, the satellite-line photons are almost never reabsorbed because the density of the excited ions, which are necessary for the reabsorption, is rather low.

To sum up, the photons of resonance lines are often reabsorbed and reemitted during the transfer from the plasma center to the detector (thus mostly carrying information about the plasma edge), while the satellite lines carry information directly from the place they have been first emitted.

The multiple-excited ions can originate in several processes. One of them is the *dielectronic recombination*, when a free electron is captured into an ionic excited state and the released energy is transfered to the bound electron, which is then also excited. The other way is the *impact excitation*, which may occur twice or more times in a short time period, thus resulting in the multiple excitation of the ion.

3 Double-foil experiments

Here we describe the basic scheme of the double-foil laser-plasma interaction experiments, which forms a [redacted] of our project.

The principle of the experiment consists in laser irradiation of the target placed in a vacuum vessel, and the analysis of the x-ray emission accompanying the laser-matter interaction. The target consists of two thin intermediate-Z foils (usually 0.8 μm Al and 2 μm Mg) with variable spacing (usually $200 - 500$ μm).

As the laser beam impinges on the target, it produces a plasma on the first irradiated foil. The plasma jet expands perpendicularly to the foil surface at both its sides. With respect to the experiment configuration used, there are two possible scenarios:

1. The plasma jet collides with the relatively cold second foil.

2. The laser beam burns through the first foil and impinges on the second foil before the first-foil plasma reaches it. Consequently, there is already a plasma plume produced on the second foil before arrival of the plasma jet and we observe the collision of those two plasmas.

The occurrence of one of these scenarios depends mainly on the laser-foil geometry, first foil thickness and composition, and on the laser beam parameters.

In some experiments, an auxiliary counter-propagating laser beam can be focused on the second foil from the other side to preheat it and thus to vary the conditions of plasma interaction. The most relevant diagnostics for these experiments is based on an analysis of the emitted x-ray radiation. There can be several types of tools providing temporal, spatial or spectral resolution or its combinations.

4 Instrumentation

In this chapter we describe the instrumentation used in the double-foil experiments performed at the PALS Research Center in Prague [2].

The PALS main laser beam is capable of delivering up to 1 kJ of energy at the fundamental wavelength 1.315 μm, which can be tripled to 438 nm. The pulse length is 250 - 300 ps.

We used two main diagnostic tools: the VJS provided high-resolution spatially-resolved spectral data, and an x-ray streak camera combined with the slit provided spatially and time -resolved measurements of plasma expansion.

4.1 Vertical-geometry Johann spectrometer

The vertical-geometry Johann spectrometer (VJS) is an x-ray spectrometer based on the principle of vertical dispersion. It provides a high-luminosity, high-resolution, one dimensionally spatially resolved spectral data. Here we will describe the basic principles of VJS, for further reference see [3], [5].

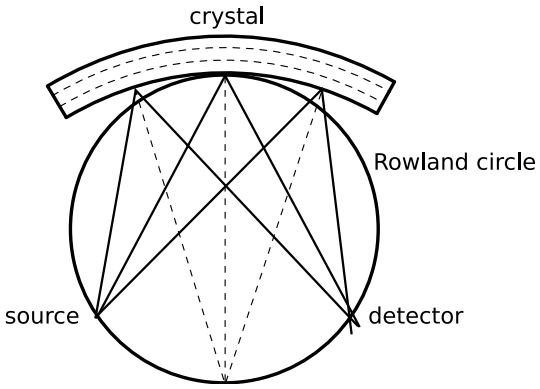

Figure 4.1: Rowland circle scheme.

The main element of VJS is a cylindrically bent crystal, which defines a Rowland circle (RC). Neglecting the focusation defects, the Rowland circle scheme (Fig. 4.1) guarantees that any ray going from the point on this circle to the crystal is reflected to another point on the RC, which is symmetrically located along the crystal axis.

This means that if the radiation is emitted from a line source lying on the RC, it is reflected and focused to the corresponding line on the RC, where a detector can be placed. In concrete experiments, neither the source nor the detector are positioned perfectly on the RC; for elongated sources, both the source and the detector are perpendicular to the central ray connecting the relevant point on the RC with the crystal center.

The dispersion is realized in the vertical direction (i.e. perpendicular to the RC plane). It is based on the Bragg's law, which states that only photons with the wavelength λ

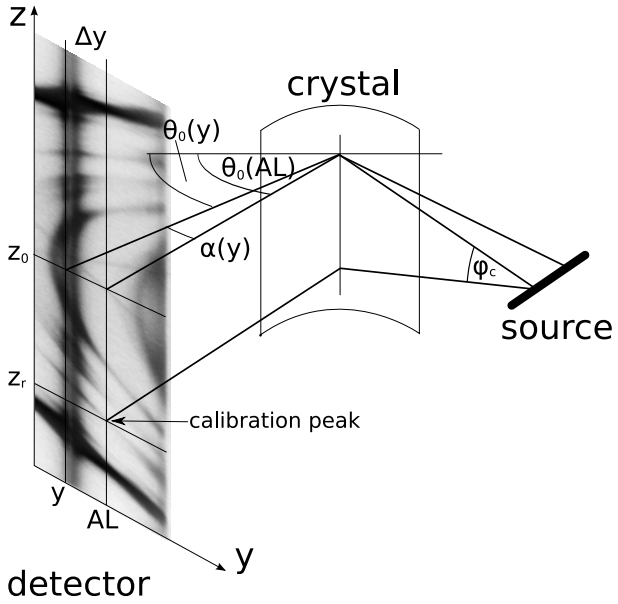

Figure 4.2: Schematic drawing of the VJS setup.

corresponding to the glancing angle θ are reflected, according to the formula

$$\lambda = \frac{2d}{n} \sin\theta, \tag{4.1}$$

where d is the spacing parameter between diffraction planes of the crystal and n is the spectroscopic order.

In our experiment, we used a crystal with the crystal spacing $2d = 0.85084$ nm and the bending radius of $r = 76.6$ mm. The spectroscopic order was $n = 1$. As the detector, x-ray film Kodak CX was used.

The schematic drawing of the VJS setup can be seen in Fig. 4.2. There is a line source on the right side of the image, which emits radiation towards the cylindrically bent crystal in the center of the image. The radiation is reflected towards the detector (on the left), where the film with recorded spectrum is drawn. In the spectrometer there is also a beam stop (not shown in the picture) preventing radiation to go directly from the source to the detector.

Figure 4.3 shows a typical scanned film from VJS with the spectrum recorded. The vertical axis of the image corresponds linearly to the spatial position of the emitted spectra, the horizontal axis corresponds to the wavelength with a more complicated relation Eq. **??**. The dominant horizontal shape represents a strong radiation emitted from the laser-irradiated foil. The conic-like lines are the spectral lines emitted at different distances from the foil surface. Their special shape is due to the VJS geometry.

4.1.1 VJS spectra reconstruction

The films with spectral records (shown in Fig. 4.3) need to be digitized, calibrated and recalculated to get relevant spectral data.

The digitization can be performed using a precise but not easily available two-dimensional densitometer. As an alternative to this process we have used a tabletop scanner Epson

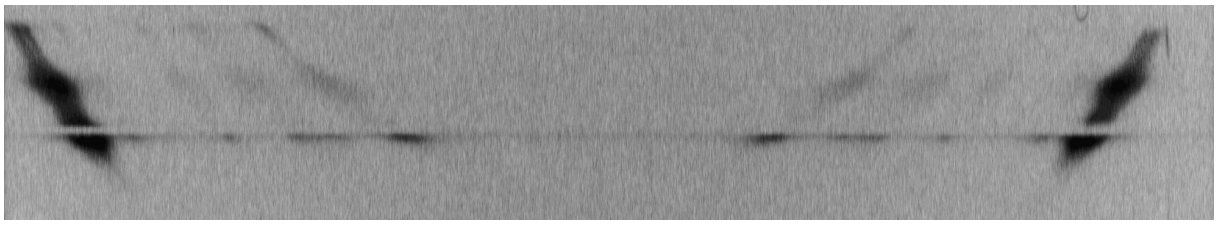

Figure 4.3: Typical scanned film from the VJS with the spectrum recorded.

Perfection V700 with the capability of scanning the films.

First, it was necessary to calibrate the scanner to the optical density, which can later be recalculated to real exposures by using the known characteristic curves of the film.

To get this calibration, we scanned the calibration wedge delivered by the x-ray film producer (Kodak). The measured values stored in the tiff format were fitted with the logarithmic function (because of the logarithmic definition of the optical density). The resulting parameters of this fit were used for the spectra reconstruction. The found dependence of the optical density on the scanned tiff value is seen in Fig. 4.4, where the points denote measured data and the line denotes their logarithmic fit.

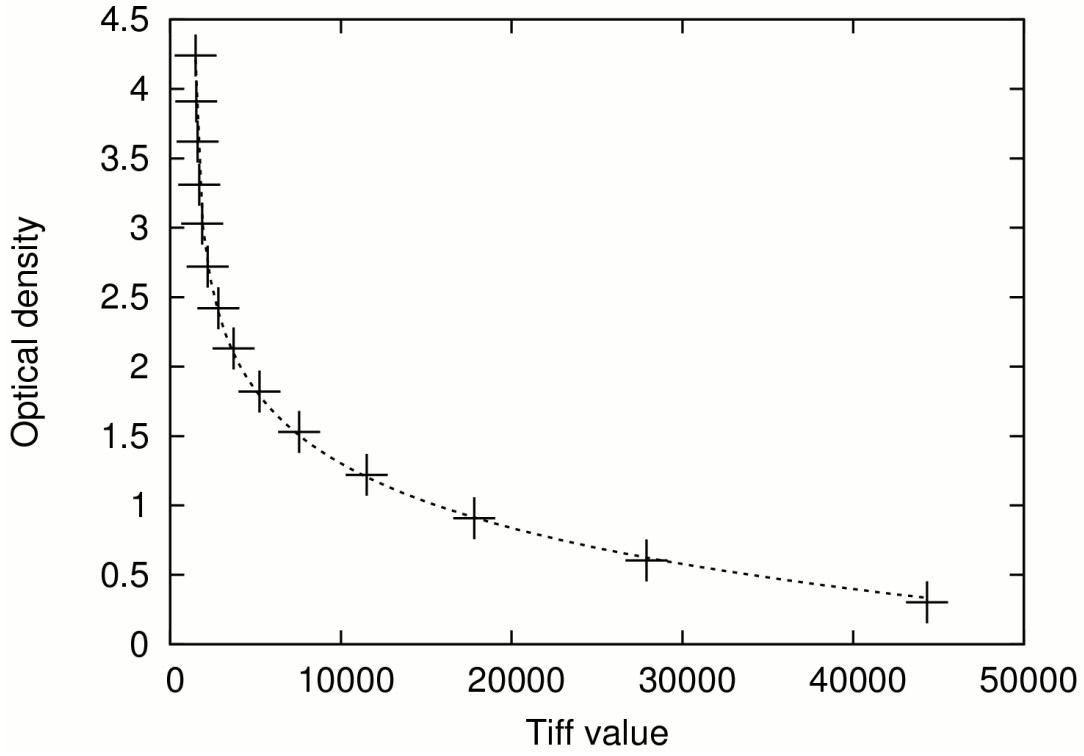

Figure 4.4: Scanner calibration - the relation between the scanned tiff values and the optical density. Points represent the measured values and the line is the fitted calibration function.

For handling the scanned films and the spectra reconstruction we developed a special software package, the *VJS Analyser*, which is described below.

4.1.2 VJS Analyser

VJS Analyser is a software package which was developed for the reconstruction and the analysis of the spectral data from VJS. It is written in the Java language.

Only the main features and capabilities of this application are described here. The details of VJS Analyser can be found in its user manual (appendix A). The illustrative picture of VJS Analyser in its spectra viewing mode can be seen in Fig. 4.5.

The input of this application is the scanned film data file or an equivalent file from densitometer, in format of 16-bit gray-scale TIFF image.

The main functions of VJS Analyser include:

- Viewing and basic manipulation of 16-bit gray-scale TIFF images.
- Precise measurement of the spectral data tilt using correllation algorithm based on the data symetry.
- Precise determination of the spectral line positions using the least square fit of the appropriate profile.
- Spectra reconstruction - conversion of the raw data into a set of calibrated spectra.
- Viewing and browsing of reconstructed spectra.
- Exporting the selected part of spectral data into a 2D plot suitable for elementary analysis or presentation.
- Exporting the spectral data into tables suitable for further analysis.

4.2 X-ray streak camera

Streak camera is a device providing data with high temporal resolution. It transforms the temporal profile of the measured signal into a 2D spatial profile on a detector. The radiation passing through the entrance slit of the streak camera is converted into electrons and then they are deflected using a strong 1D time-variable electric field. The other dimension is left unchanged, so we get an image with one axis corresponding to time and the other axis corresponding to the spatial distribution of the measured signal.

We used Kentech low-magnification x-ray streak camera with temporal resolution 2.03 ps/pixel and spatial resolution 2.9 μm/pixel. An image from this streak camera can be seen in Fig. 7.3.

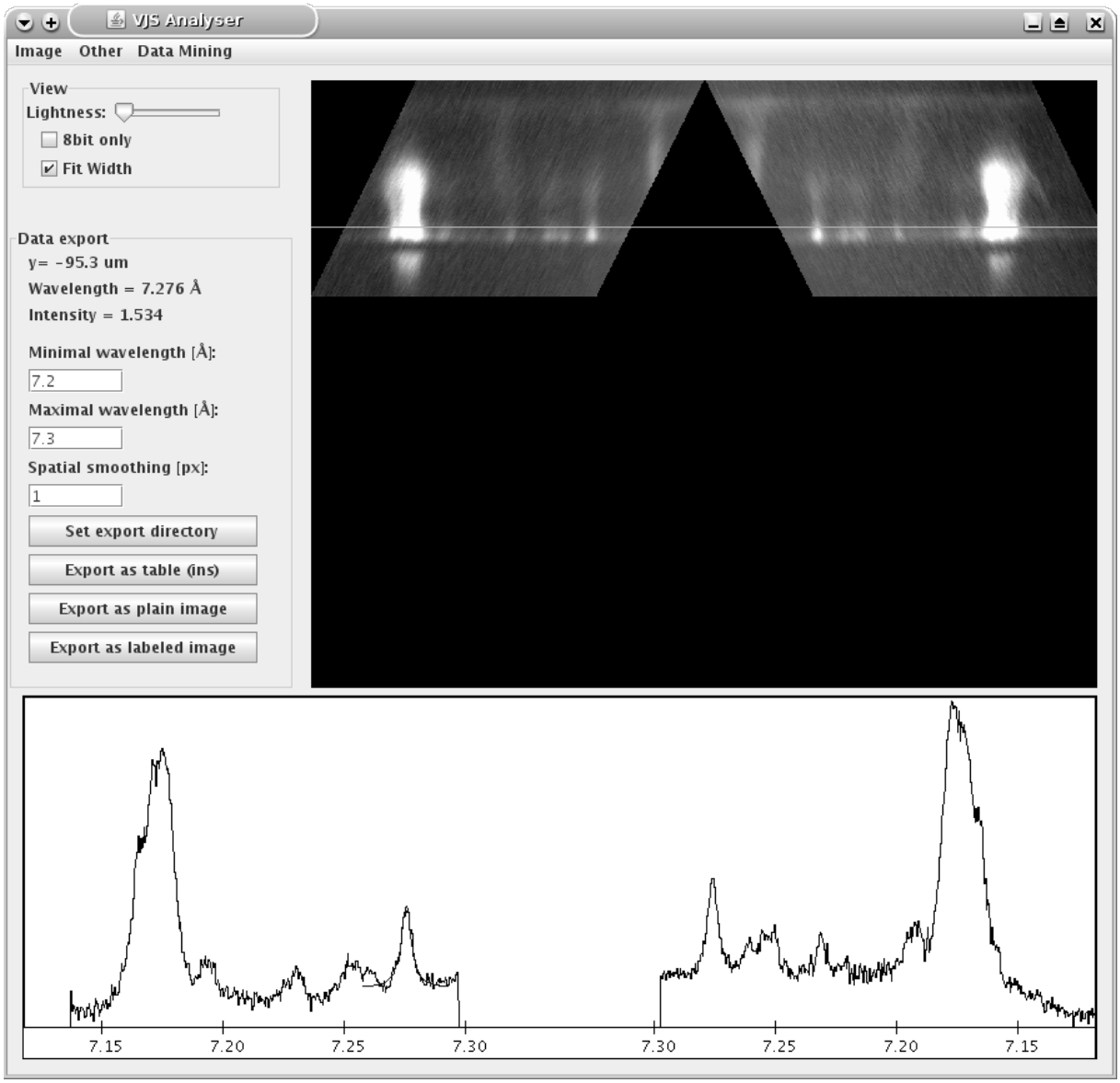

Figure 4.5: Preview of the spectra analysing regime of the VJS Analyser.

5 Theoretical spectra

Theoretical x-ray emission spectra of hot dense plasma provides a very powerful tool for plasma diagnostics. The measured experimental data can be directly compared to a set of theoretical spectra and thus the free parameters of the simulation can be estimated.

The cruical part of the spectra synthetization process is the calculation of plasma population distribution, which can be calculated using several models used for different regimes of plasma parameters. The Coronal equilibrium model (CE) gives the best results for diluted plasmas, while the local thermodynamical equilibrium (LTE) model is useful for dense, equilibrium matter. For our purposes, the intermediate Collisional Radiative model (CR, or non-LTE) is the only possible choice because it can handle non-equilibrium plasmas within huge range of densities[1].

While the first two models get the population distribution from basic principles, the CR model formulates a set of rate equations [8]

$$\frac{\mathrm{d}n_\mathrm{i}}{\mathrm{d}t} = -n_\mathrm{i} \sum_{\mathrm{j,j\neq i}} W_\mathrm{ij} + \sum_{\mathrm{j,j\neq i}} n_\mathrm{j} W_\mathrm{ij}, \tag{5.1}$$

where n_i is the ion population in the ith state, and the W_ij is the transition coefficient between the atomic states i and j. This coefficient is a sum of rates for all included atomic processes, and may be dependent on plasma parameters, population of atomic states and radiation intensity.

These equations need to be completed with the *radiation transport equation*, which is a relation between the intensity of radiation in each point of plasma and the plasma emisivity and absorptivity coefficients (which indicates the radiation emission and absorption, respectively, of given wavelength per unit time and volume), which are dependent on ion population distribution. These two sets of equations need to be solved numerically together.

The radiation transport can bring new effects to experimental spectra, which do not follow from simple dimension-less theories, like opacity broadening or other line-shape modifications.

5.1 Opacity broadening

In this section, I would like to give a brief description and explanation of the *opacity broadening*, one of the simplest and most noticable effects of the radiation transport.

The radiation transport equation can be simplified for stationary homogenous 1D plasma as[6]

$$\frac{\mathrm{d}I}{\mathrm{d}\tau} = \frac{\varepsilon}{\kappa} - I, \tag{5.2}$$

where $\varepsilon(\nu)$ and $\kappa(\nu)$ are the emissivity and absorptivity, $\tau(z,\nu)$ is the optical depth defined as $\tau(z,\nu) = \int_0^z \kappa(z',\nu)dz'$ with the spatial coordinate z, and the $I(\nu, z(\tau))$ is the radiation intensity.

The solution for plasma with thickness L is

$$I = \frac{\varepsilon}{\kappa}(1 - e^{-\tau}) = \frac{\varepsilon}{\kappa}(1 - e^{-\kappa L}). \tag{5.3}$$

For radiation with low optical depth ($\tau = \kappa L \ll 1$), the exponential can be expanded into lowest orders Taylor series and the equation is simplified as

$$I = \varepsilon L, \tag{5.4}$$

thus the emission is proportional to emissivity; for optically thick lines, the emission is decreased by the exponential function and the intensity is limited by the factor $\frac{\varepsilon}{\kappa}$, called the *source function*, which is, for LTE plasmas, equal to the black-body radiation, thus not having the significat spectral dependence as emissivity or absorptivity.

This explains why the intensity of strong spectral lines, which have large optical depth, is decreased due to their reabsorption on its way throguh the plasma, while the optically thin satellite structure is unperturbed.

The effect is illustrated on theoretical profiles of $Si0_2$ plasma with ion density $n_\mathrm{i} = 8 \times 10^{20}$ cm^{-3}, temperature $T = 350$ eV, and thickness $L = 100$ μm, relevant to experiments described in chapter 6.

Fig. 5.1(a) shows the emissivity, which corresponds to the emission intensity for thin plasmas. Fig. 5.1(b) shows the optical thickness, (and also the absorptivity, because they are proportional to each other.) The optical depth of $Si0_2$ He_α resonance line (at ~ 6.18 Å) is ~ 10 thus this transition is strongly affected by the reabsorption, while for the satellite structure with depth less then ~ 0.1 the optically thin limit can be used. Fig. 5.2 shows the emission profile of the plasma (with linear scale in contrast to previous profiles) with the resonant line reabsorped, thus decreased.

The huge difference between satellite and parent intensities in the absorptivity profile (compared to emissivity profile) is caused by the fact that the absporption of light with the satellite-line wavelength is done on excited ions, which have much less populations in plasma than ground state ions need for resonance-line absorptions.

5.2 Comparison of various simulation codes

For our evaluation we could use the *FlyCHK* and *PrismSpect* codes. By direct comparison of relevant theoretical spectra produced by these codes we realized, that the PrismSpect comprises more atomic data as demonstrated in more complex satellite structure, so we decided to use this one.

Second step was to compare the selected code PrismSpect with the *Maria* code that was used in previous publications[7] to acquire parameters from the LPWI experiments performed in 2006, so we fitted the same experimental data using the *PrismSpect* theoretical spectra and compared the resulting parameters.

In Fig. 5.3 there are three experimental spectra (black triangles), fitted using the Maria code (blue line) and using the PrismSpect simulations (red lines). The temperature and electron density of the fits are in talbe 5.1. The Maria simulations were performed on plasma with various thicknesses and considering plasma gradients, while the PrismSpect simulations were performed on homogenous, 100 μm thick plasma.

The result of the comparison is quite satisfactory, the differences between plasma parameters are acceptable.

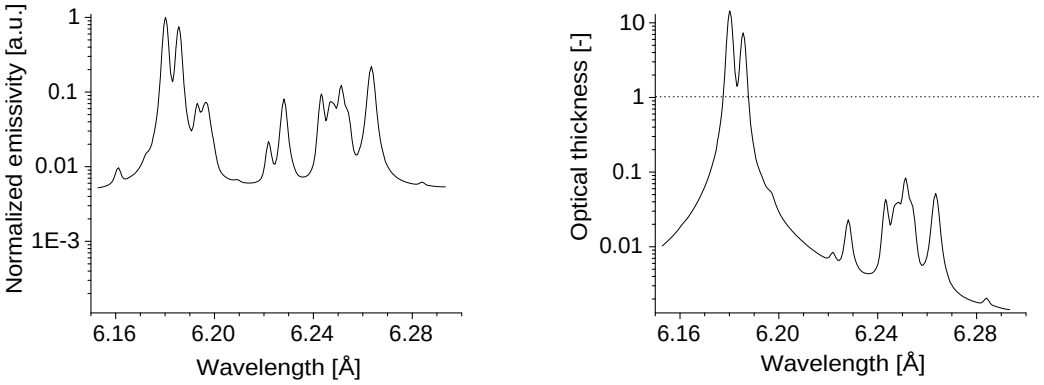

(a) (b)

Figure 5.1: Emissivity (a) and absorptivity (b) of $Si0_2$ plasma with $T = 350$ eV, $n_i = 8 \times 10^{20}$ $\frac{\text{ions}}{\text{cm}^3}$.

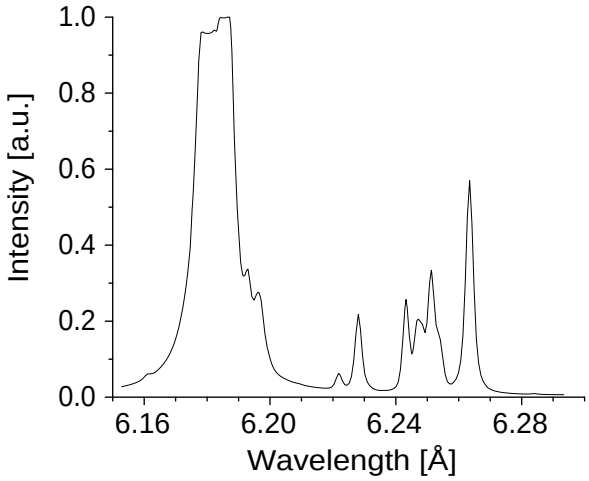

Figure 5.2: Intensity spectrum of 100 µm thick plasma.

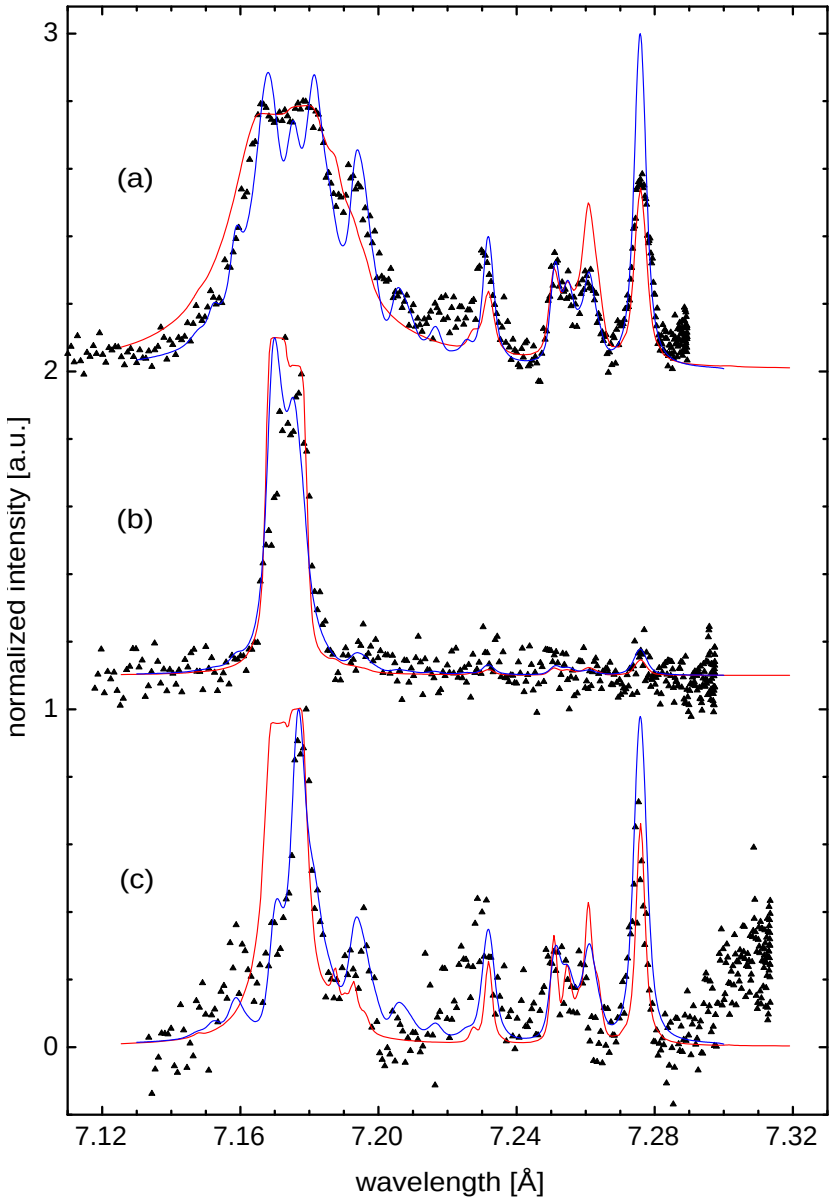

Figure 5.3: Comparison of fitted theoretical profiles; Experimental spectra (black triangles) were fitted using Maria code (blue line) and PrismSpect code (red line)
.

	Maria		PrismSpect	
spectra	T [eV]	n_e [e/cm^3]	T [eV]	n_e [e/cm^3]
(a)	300	3×10^{21}	460	1×10^{22}
(b)	700	3×10^{20}	760	1×10^{21}
(c)	220	$(1 \div 3) \times 10^{21}$	220	5×10^{21}

Table 5.1: Parameters of Maria and PrismSpect fits.

5.3 Method of experimental and theoretical spectra comparison

Although the PrismSpect code has the capability to compare simulated and experimental spectra, it is not suitable to find the best fitting theoretical spectrum to selected experimental one, so I have developed a new application for this purpose, called *CompSpect*.

The PrismSpect provides funcionality of creating a set of spectra with various temperatures and densities. This set is loaded into the CompSpect application as well as the experimental data, which can be either single spectrum, or a set of spatially resolved spectra, eg. from the VJS Analyser code.

The application uses a least square method to determine which simulated spectra is best fitting to the experimental one. However, this method did not gave sufficient results so a possibility to easily select the best spectra manually was also included.

Though the original idea was to improve the fitting algorithm to search the best spectra autmatically with good enough results, finally I realized there were serious reasons why it would be too complicated, so in current version the use of automatical search is recomended only as an initial fit for manual search. The reasons were:

- Difficulties with determining the minimum and maximum intensity in the spectra caused by noise.
- In some cases it is more important to fit the integrated intesity of a line, than its whole profile. This is not possible to perform using least square fit, instead of it it would be necessary to perform spectra deocmposition.
- Different parts of spectra may have various importance (weights) for fitting.
- In spatially resolved spectra, we use the assumption of continuous and/or monotonous evolution of plasma parameters with distance, which would be more difficult to implement in automatic fitting.

The preview of main window of CompSpect application is in Fig. 5.4. It is a *Java* application, so it can be used on any computers hosting a Java Virtual Machine. Its user manual is in appendix B.

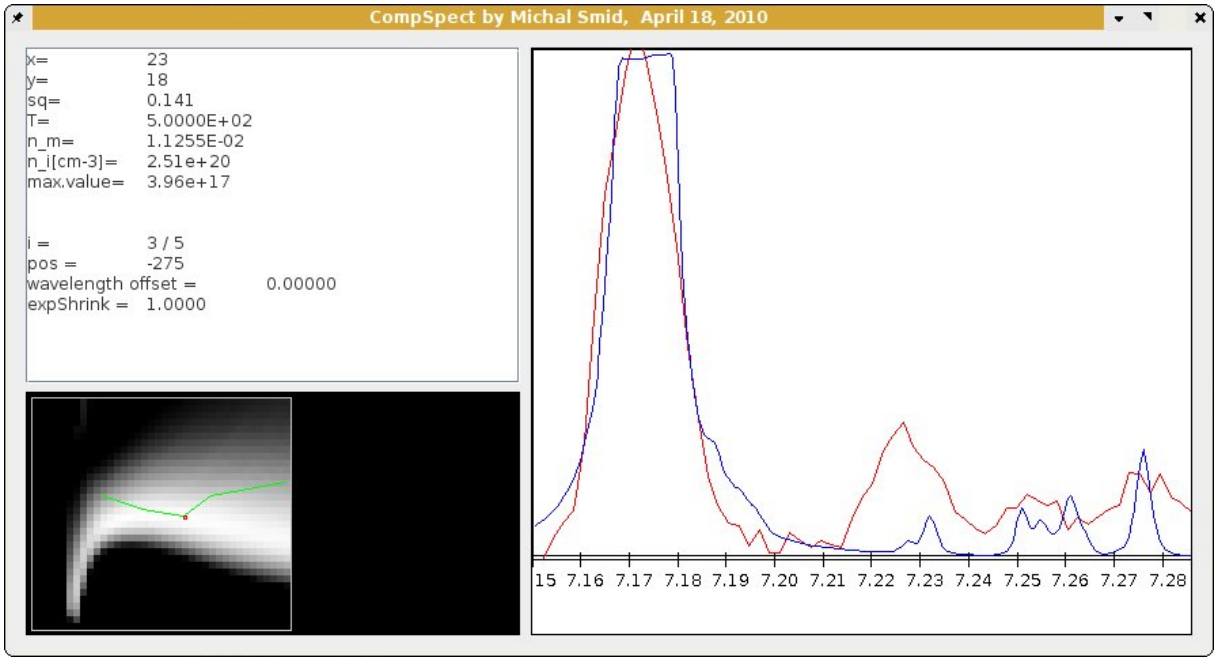

Figure 5.4: Screenshot of the CompSpect application.

6 $Si0_2$ experiments

This chapter describes a set of experiments performed in January 2009 with prof.Limpouch in PALS laser laboratory, which were evaluated using the spectra fitting method as described above.

The experiments were similar to those described in chapter 3, the main difference was in the target material and structure. Here we used two types of $Si0_2$ targets:

1. Massive $Si0_2$ target. The laser focal spot had diameter 80 μm.

2. $Si0_2$ dot with diameter 100 μm and thickness 1 μm fixed on a poly(methyl methacrylate) (PMMA) base. Focal spot was ∅ 250 μm.

The target was irradiated by the PALS main beam with puls length $\approx$ 250 ps, wavelength $\lambda = 1.315$ μm, energy $\approx$ 70J and focal spot various for different targets.

The main diagnostic tool was the VJS spectrometer, set up to observe the He_α or Ly_α lines with their satellite structures, and providing spatial resoultion along the laser axis. The VJS spectral record from one of the dot target experiments is shown in Fig. 6.1. The preview of its spectrum in distance 16 μm from the surface compared to assigned theoretical one is in Fig. 6.2.

The CompSpect code was used to assign plasma parameters using spectra fitting to profiles from various distances from the target surface. The resulting temperature and density profiles for the massive target and for the dot target experiments are in Fig. 6.3.

In both profiles we can see a significant decrease in density and almost linear increase of temperature with distance from the target. The main difference between both variants of experiments is the greater increase of temperature in the massive target experiment, which may be caused by two reasons:

- Higher intensity of the laser. (The same total intensity was focused on smaller diameter.)

- The massive target could absorb the whole duration of laser pulse, while the 1 μm thin $Si0_2$ dot absorped only part of the pulse before it get ionized and diluted.

In the dot target experiment, the plasma radiation was observed till higher distances from the target (up to $\sim$ 100 μm), which can be explained by confining of the Si plasma with surrounding PMMA plasma. (The $Si0_2$ plasma could not spread in directions perpendicular to laser axis.)

6.1 Rotation of targets

Some experiments from this series were performed with target rotated 30° to laser axis, towards direction of spectra observation, to analyze the possibilites of similarly rotated double-foil LPWI experiments.

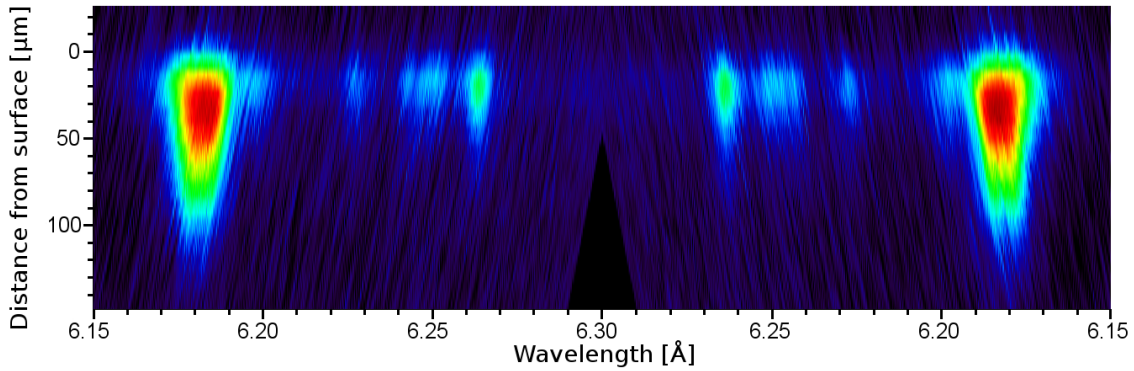

Figure 6.1: Spatially resolved spectra from the VJS spectrometer for the $Si0_2$ dot experiment.

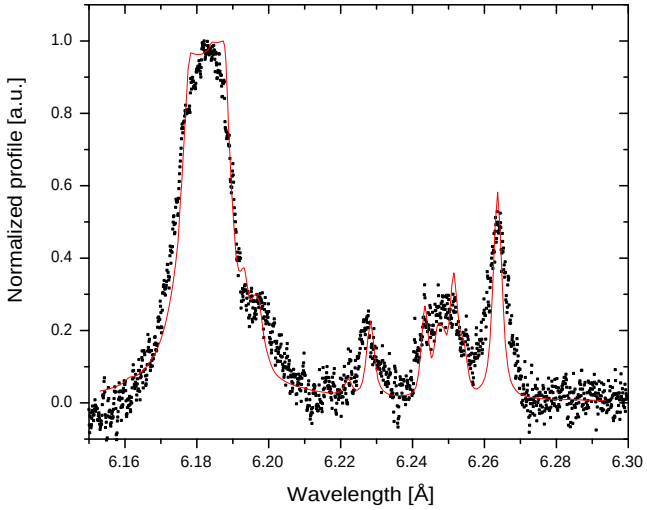

Figure 6.2: Experimental profile (black dots) and the best fitted simulated spectra (red line) from the $Si0_2$ dot target experiment, 16 µm from the target surface.

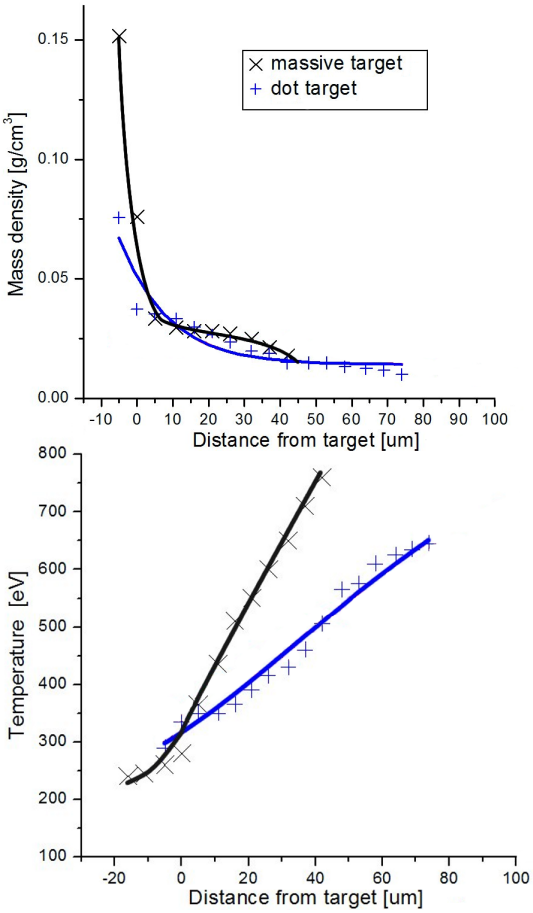

Figure 6.3: Temperature and density variations with distance in $Si0_2$ experiments, for two types of targets.

According to simulations [7], the plasma should stream perpendicular to the target surface, so the rotation of the target should be measureable through the doppler shift of the lines. The measurement was performed on the optically thin J-satellite, because it is not reabsorped, thus giving us information from the whole plasma stream, while the observed emission of the resonance line is produced mainly in the plasma edge.

The point of the measurement was to take two similar shots with different target rotation and measure the difference in J-satellite wavelength. The typical approach of VJS calibration (to define a wavelength of one line) was useless here, because for this purpose there was no line unaffected by the target rotation and thus by the doppler shift.

We used a fact that VJS provides two symetrically located set of spectra (as illustrated in Fig. 6.4), and for the distance z between two records of one spectral line with wavelength λ there is a relation (as described in VJS Analyser manual in Appendix A)

$$z = 2l \tan(\mathrm{acos}(\frac{\lambda}{\lambda_0(y)})), \tag{6.1}$$

where l is the plasma – crystal – detector distance, $\lambda_0(y)$ is the wavelength corresponding to the central point on the film in given spatial position y and should be the same for both experiments, if the experimental setup is kept untouched.

The measured distances were $z_\mathrm{p} = 19.05$ mm for perpendicular target and $z_\mathrm{r} = 19.48$ mm for rotated target, so the difference is $\Delta z = 0.43$mm. The λ_0 was calculated from the Eq. 6.1 with the tabulated value of J satellite $\lambda = 6.7422$ Å and z from the perpedicular experiment, which is unperturbed by the Doppler shift. Distance l is $l = 121.928$ mm. This gives the $\lambda_0 = 6.7627$ Å and with this value we get the wavelenegth for rotated target as $\lambda_\mathrm{r} = 6.7412$ Å, getting the perturbation of wavelength as $\Delta\lambda = \lambda - \lambda_r = 0.97$ mÅ.

6.1.1 Uncertainty estimation

We identified three sources of uncertainties in the peak distance measurement:

1. Unprecise idnetification of the target surface on the scanned film; The distance between lines is strongly dependent on the y coordinate on the film. For given wavelength and position the change of distance z with position y is $\frac{\mathrm{d}z}{\mathrm{d}y} \approx 17$. The uncertainty of correct identification of surface position is approximately 1 px on the scanned film, that is $\sim$ 6 μm, so we get uncertainity $\epsilon_1 = 0.1$ mm

2. Position of the target; Possible imprecision of target positioning was estimated as 10 μm, the effect of target position would affect the distance the same way as its unprecise identification mentioned above, this source gives $\epsilon_2 = 0.01 \times 17 = 0.17$ mm.

3. Measurement of the distance between lines; Cruical problem of the distance measurement was precise peak idnetification, which was complicated due to overlap of two lines, the uncertainty was estimated as $\epsilon_3 = 0.1$ mm

Adding these uncertainties, we get $\Delta z = 0.3 \pm 0.2$ mm. Converting to wavelength scale using Eq. 6.1 we get

$$\Delta\lambda = 1.0 \pm 0.4 \text{ mÅ}. \tag{6.2}$$

This gave us important information on the possibilities of similar measurements in the ongoing summer 2010 experiments.

The Doppler shift relation $\Delta\lambda = \lambda \sin(\alpha)\frac{v}{c}$ implies the plasma near surface velocity $v \approx 10^5 \frac{m}{s}$, which is well in agreement with 1D hydrodynamic simulations of similar arrangement[4].

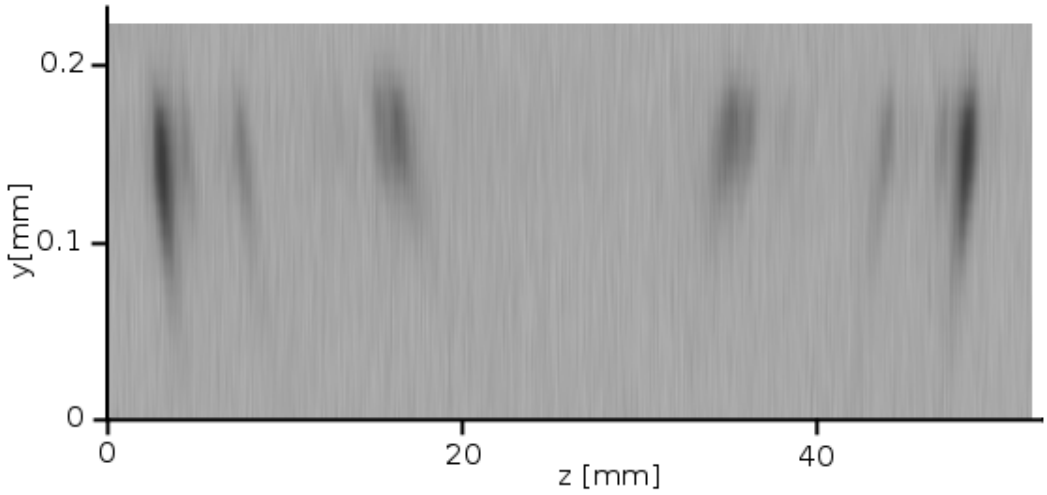

Figure 6.4: Raw VJS record of the $Si0_2$ dot experiment.

7 LPWI experiments evaluation

In this chapter we present the evaluation of the LPWI epxeriments performed in January 2009, as described in chapter 3. In the first section we present a basic description of measured data and their comparison with older experiments, as was written for my bacheolr thesis, while in the second section we apply the methods of theoretical spectra fitting and present its results, as a original work for my research project.

7.1 Comparison to 3Ω experiments.

We compare the 2009 experimental results with the similar one performed in 2006, described in [7].

Both experiments used double foil targets irradiated from the Al side only. The VJS was set to measure the Al Ly$_\alpha$ resonance line with its satellites, especially with the J satellite at 7.2759 Å. Table 7.1 compares the most important experimental parameters. The reconstructed x-ray spectra are shown in Figures 7.1 and 7.2.

	2006	2009
Target material	Al/Mg	Al/Al
Foil spacing	350 μm	450 μm
Laser beam intensity	79 J	112 J
Laser beam frequency	438 nm	1315 nm

Table 7.1: Comparison of the experimental parameters.

In the lower part of Fig. 7.1 (2006 experiment) we can see spectra emitted from the Al foil (positioned at the distance of 0 μm) and those close to the Mg foil viewed on the top (at $\sim$ 350 μm). The outer couple of intensive lines corresponds to the resonant Al Ly$_\alpha$ line, the less intensive couple in the middle (at $\sim$ 7.27 Å) to the J satellite. We can see the emission of the full group of the satellite lines from the Al foil, their disappearance at about 150 μm and their reappearance at the Mg foil. This corresponds well to the record from the streak camera (Fig. 7.3), where the emission from the first foil starts at $\sim$ 0.2 ns, and at $\sim$ 1 ns occurs the interaction of the Al plasma with the plasma generated from the Mg foil.

The spectra shown in Fig. 7.4 (2009 experiment) correspond to the altered experimental configuration. The striking differences include:

- The gap in the line emission close to the position of the Al foil. This is explained by a small tilt of this foil, which partly blocks the radiation. (The laser beam was focused at the distance of approximately 200 $\div$ 500 μm from the foil edge.)
- The spectral lines display distinct second maximum in between the foils (at $\sim$ 200 μm), while close to the second foil they do not reappear so significantly.

The strong emission at the midplane of the foils is again explained by a collision of two counter-streaming plasma jets. The plasma jet from the second foil was produced by the laser beam that burned through the first foil.

The observed difference corresponds to the diverse experimental conditions, in particular to the significant difference in laser frequency, which alters substantially the mechanism of energy deposition in the foils.

To summarize, in the first experiment the plasma jet collision with relatively cold Mg foil was observed, while in the second one we had observed the collision of two plasma jets.

7.2 Fitting with theoretical spectra

For this evaluation, we took an Al/Mg target experiment, with laser energy $E = 193$ J. The record from VJS spectrometer is shown in Fig. 7.4, the significant profiles from this data are drawn and described in Fig. 7.5.

In the lower part of Fig. 7.4 we can see spectra emitted from the Al foil (positioned at the distance of 0 μm), and those close to the Mg foil viewed on the top ($\sim$ 550 μm). The outer couple of intensive lines corresponds to the resonant Al Ly_α line, the less intensive inner couple on the Al foil to the Al Ly J-satellite($\sim$ 7.27 Å). The horizontal line with no radiation at $\sim$ 0 μm is the shade made by the the unperturbed part of the Al foil. We can see the emission of the full group of the satellite lines from the Al foil spreading and damping on both its sides, and their intensification at $\sim$ 200 μm, where they are also mixed with the Mg_δ ($\sim$ 7.31 Å) and Mg_ϵ ($\sim$ 7.22 Å) lines due to the collission of the counter-streaming plasma jets and consequently the density buildup in this region. The Al emission structrue disappear above $\sim$ 500 μm, except for the weak J-satelliteand the resonance line. On the Mg foil ($\sim$ 550 μm), we can see distinct Mg lines, as well as the Al J-satelliteand the resonance line, which gave a clear evidence of Al plasma penetration into this region.

In Fig. 7.5 there are five selected distinctive spectra from the measured range, fitted with PrismSpect simulation profiles with plasma parameters summarized in Tab. 7.2. It shows a typical plasma diluting with increasing distance from both foils.

The effect visible on Mg He_δ line at 555 μm may be caused by the non-homogenity of the plasma, where the optically thick resonance line is reabsorped with smaller line width then it was emited[6], thus producing the specific splited shape of the line.

The midplane spectrum (190 μm) shows Al emission as well as the Mg He_ϵ line. The Mg He_δ line is not visible because it is out of the spectrometer range in this position. (The measured range of VJS varies with the distance from target, as seen on Fig. 7.4.) The resonance line is strongly reabsorped, thus providing no relevant information, while the satellites shows distinctive line broadening, which may be caused either by higher temperature (>1 keV), higher density or plasma unhomogenity.

The difficulties with fitting these data are produced mainly with the time and spatial integration.

distance [µm]	Material	T [eV]	n_m [g/cm^3]
21	Al	300	0.02
95	Al	480	0.01
344	Mg	200	0.005
555	Mg	200	0.02

Table 7.2: Parameters of Maria simulation spectras fited onto LPWI experiment.

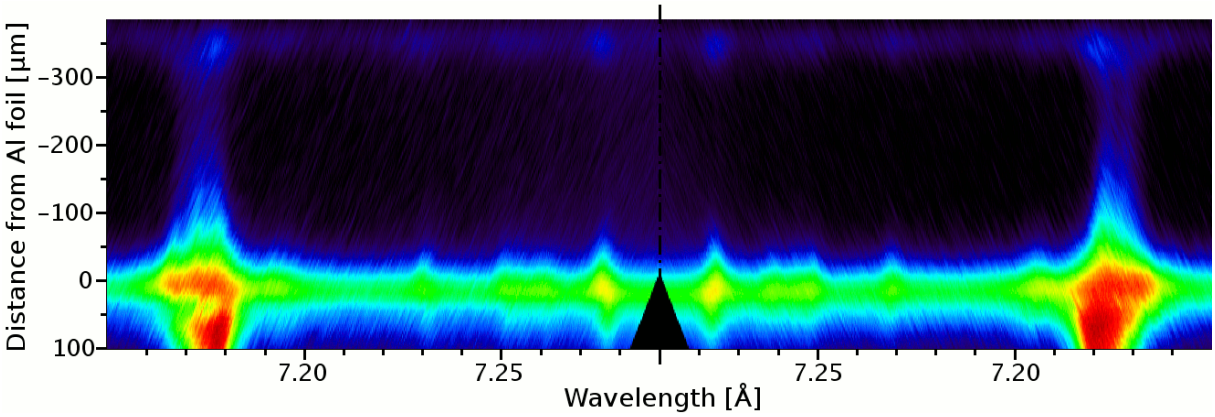

Figure 7.1: Spatially resolved spectra of the 2006 experiment.

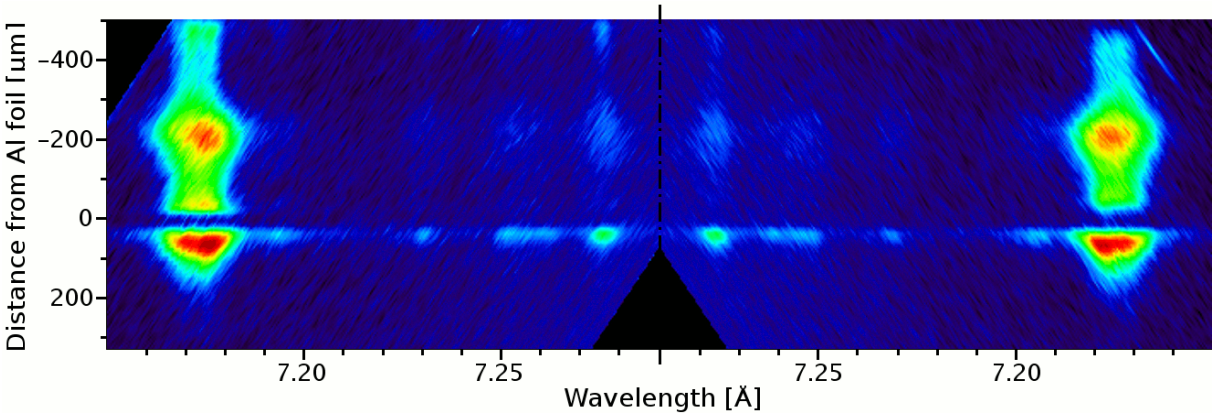

Figure 7.2: Spatially resolved spectra of the 2009 experiment.

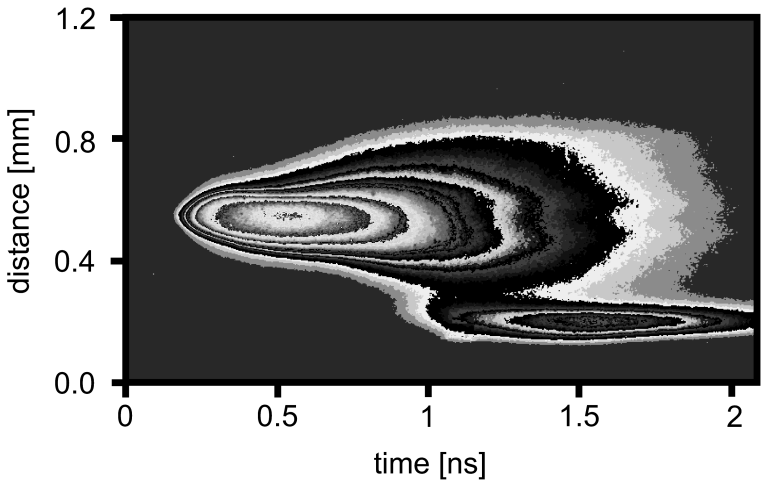

Figure 7.3: Spatially and temporally resolved emission from the streak camera of the 2006 experiment.

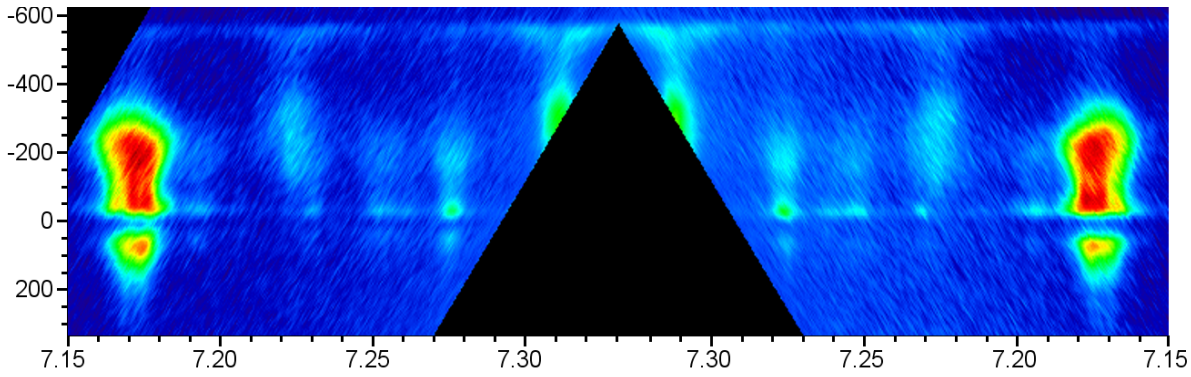

Figure 7.4: Spatially resolved spectra of the LPWI experiment.

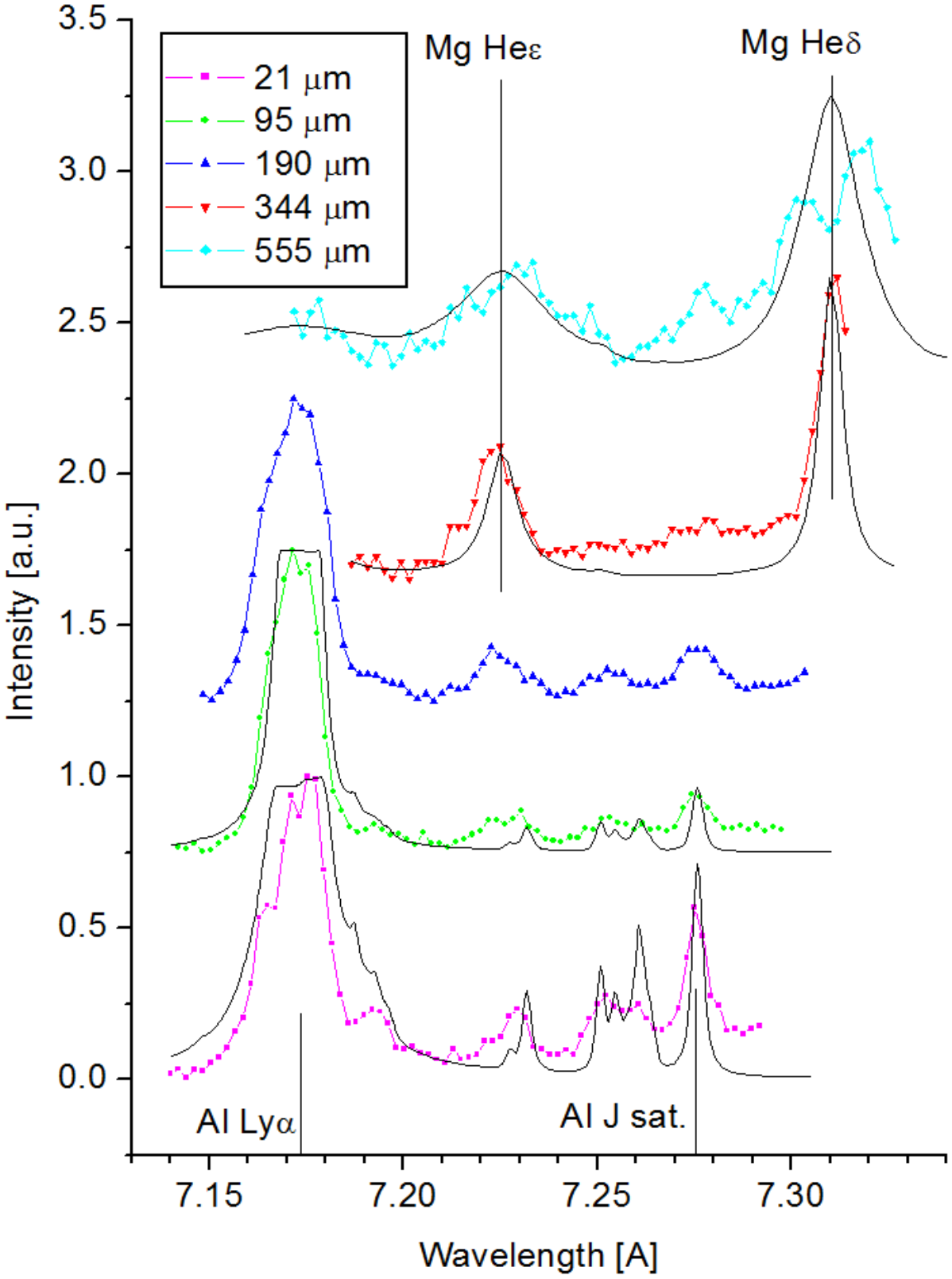

Figure 7.5: Selected spectra from LPWI experiment.

8 Conclusion

The first part of this research project report summarizes very briefly the problematics of plasma-wall interaction and demonstrates the possibility of its studies through the double-foil laser-plasma wall interaction experiments. The basic properties of instruments used in relevant experiments are presented, and the results obtained by the novel code for reconstruction of the measured spectra are shown.

The second part concerns the theoretical spectra simulations and their use as a diagnostic method, for which a novel code has been developed, and also its application for relevant LPWI experiments.

I should emphasize that the measured high-resolution spectra can provide much more information on plasma interaction than the results discussed in this thesis. In particular, there is a substantial information potential in the satellite lines widths and positions depending on the spatial range of their emission. Further analysis of this data will be a subject of future investigation.

My personal contribution to this topic can be summarized in few points:

- Participation in experiments performed in January 2009.
- Design of the alternative approach to the VJS spectra processing. That consists of the spectra digitizing including the scanner calibration, and of design, testing and application of the novel *VJS Analyser* software package for spectra reconstruction, including its manual for its easy use (appendix A).
- Creating the easy-to-use codes for theoretical to experimental spectra comparing and fitting.
- Applying these codes for basic evaluation of the 2009 LPWI experiments.

A VJS Analyser manual

B CompSpect manual

Bibliography

[1] D. Salzmann. *Atomic Physics in Hot Plasmas*. Oxford University Press, 1998.

[2] A. Cejnarova, L. Juha, B.Kralikova, J. Krasa, E.Krousky, P.Krupickova, L.Laska, K.Masek, T.Mocek, M.Pfeifer, A. Präg, O.Renner, K.Rohlena, B.Rus, J.Skala, P.Straka, J.Ullschmied, and K. Jungwirth. The Prague Asterix laser system. *Phys. Plasmas*, 8:2495, 2001.

[3] O. Renner, T. Missalla, P. Sondhauss, E. Krouský, E. Förster, C. Chenais-Popovics, and O. Rancu. High-luminosity, high-resolution, x-ray spectroscopy of laser-produced plasma by vertical-geometry johann spectrometer. *Rev. Sci. Instrum.*, 68 (6):2393, June 1999.

[4] O. Renner, P. Sondhauss, O. Peyrusse, E. Krouský, R. Ramis, K. Eidmann, and E. Förster. High-resolution, measurements of X-ray emission from dense quasi-1D plasma: Line merging and profile modification. *Laser and Particle Beams.* 17 (3):365, 1999.

[5] O. Renner. *Pokročilá rentgenová spektroskopie vysokoteplotního hustého plazmatu.* PhD thesis, Insitute of Physics, AS CR, 1998.

[6] F.B. Rosmej. *X-ray emission spectroscopy and diagnostics of non-equilibrium fusion and laser produced plasmas*, in R.Hutton (Ed.), Highly Charged Ions, Taylor and Francis, to be published 2011, ISBN 9781420079043.

[7] O.Renner, F.B.Rosmej, P.Adámek, E.Dalimier, A.Delserieys, E. Krouský, J.Limpoucch, R.Liska, D.Riley, and R.Scott. Spectroscopic characterization of ion collisions and trapping at laser-irradiated double-foil targets. *High Energy Density Physics*, 3:211, 2007.

[8] H.K.Chung, R.W.Lee, M.H.Chen, and Y.Ralchenko. *The How To For FLYCHK* . URL:http://nlte.nist.gov/fly/ [cit. 2010-01-10].